A&A 596, A109 (2016)
DOI: 10.1051/0004-6361/201629022

Astronomy & Astrophysics

Planck intermediate results

XLVIII. Disentangling Galactic dust emission and cosmic infrared background anisotropies

Planck Collaboration: N. Aghanim[47], M. Ashdown[57,4], J. Aumont[47], C. Baccigalupi[68], M. Ballardini[24,39,42], A. J. Banday[78,7], R. B. Barreiro[52], N. Bartolo[23,53], S. Basak[68], K. Benabed[48,77], J.-P. Bernard[78,7], M. Bersanelli[27,40], P. Bielewicz[66,7,68], L. Bonavera[13], J. R. Bond[6], J. Borrill[9,74], F. R. Bouchet[48,73], F. Boulanger[47], C. Burigana[39,25,42], E. Calabrese[75], J.-F. Cardoso[60,1,48], J. Carron[18], H. C. Chiang[20,5], L. P. L. Colombo[16,54], B. Comis[61], F. Couchot[58], A. Coulais[59], B. P. Crill[54,8], A. Curto[52,4,57], F. Cuttaia[39], P. de Bernardis[26], G. de Zotti[36,68], J. Delabrouille[1], E. Di Valentino[48,73], C. Dickinson[55], J. M. Diego[52], O. Doré[54,8], M. Douspis[47], A. Ducout[48,46], X. Dupac[31], S. Dusini[53], F. Elsner[17,48,77], T. A. Enßlin[64], H. K. Eriksen[50], E. Falgarone[59], Y. Fantaye[30], F. Finelli[39,42], F. Forastieri[25,43], M. Frailis[38], A. A. Fraisse[20], E. Franceschi[39], A. Frolov[72], S. Galeotta[38], S. Galli[56], K. Ganga[1], R. T. Génova-Santos[51,12], M. Gerbino[76,67,26], T. Ghosh[47], Y. Giraud-Héraud[1], J. González-Nuevo[13,52], K. M. Górski[54,80], A. Gruppuso[39,42], J. E. Gudmundsson[76,67,20], F. K. Hansen[50], G. Helou[8], S. Henrot-Versillé[58], D. Herranz[52], E. Hivon[48,77], Z. Huang[6], A. H. Jaffe[46], W. C. Jones[20], E. Keihänen[19], R. Keskitalo[9], K. Kiiveri[19,35], T. S. Kisner[63], N. Krachmalnicoff[27], M. Kunz[11,47,2], H. Kurki-Suonio[19,35], J.-M. Lamarre[59], M. Langer[47], A. Lasenby[4,57], M. Lattanzi[25,43], C. R. Lawrence[54], M. Le Jeune[1], F. Levrier[59], P. B. Lilje[50], M. Lilley[48,73], V. Lindholm[19,35], M. López-Caniego[31], Y.-Z. Ma[55,69], J. F. Macías-Pérez[61], G. Maggio[38], D. Maino[27,40], N. Mandolesi[39,25], A. Mangilli[47,58], M. Maris[38], P. G. Martin[6], E. Martínez-González[52], S. Matarrese[23,53,33], N. Mauri[42], J. D. McEwen[65], A. Melchiorri[26,44], A. Mennella[27,40], M. Migliaccio[49,57], M.-A. Miville-Deschênes[47,6], D. Molinari[25,39,43], A. Moneti[48], L. Montier[78,7], G. Morgante[39], A. Moss[71], P. Natoli[25,3,43], C. A. Oxborrow[10], L. Pagano[26,44], D. Paoletti[39,42], G. Patanchon[1], O. Perdereau[58], L. Perotto[61], V. Pettorino[34], F. Piacentini[26], S. Plaszczynski[58], L. Polastri[25,43], G. Polenta[3,37], J.-L. Puget[47], J. P. Rachen[14,64], B. Racine[1], M. Reinecke[64], M. Remazeilles[55,47,1,*], A. Renzi[30,45], G. Rocha[54,8], C. Rosset[1], M. Rossetti[27,40], G. Roudier[1,59,54], J. A. Rubiño-Martín[51,12], B. Ruiz-Granados[79], L. Salvati[26], M. Sandri[39], M. Savelainen[19,35], D. Scott[15], C. Sirignano[23,53], G. Sirri[42], J. D. Soler[47], L. D. Spencer[70], A.-S. Suur-Uski[19,35], J. A. Tauber[32], D. Tavagnacco[38,28], M. Tenti[41], L. Toffolatti[13,52,39], M. Tomasi[27,40], M. Tristram[58], T. Trombetti[39,25], J. Valiviita[19,35], F. Van Tent[62], P. Vielva[52], F. Villa[39], N. Vittorio[29], B. D. Wandelt[48,77,22], I. K. Wehus[54,50], A. Zacchei[38], and A. Zonca[21]

(Affiliations can be found after the references)

Received 27 May 2016 / Accepted 9 August 2016

ABSTRACT

Using the *Planck* 2015 data release (PR2) temperature maps, we separate Galactic thermal dust emission from cosmic infrared background (CIB) anisotropies. For this purpose, we implement a specifically tailored component-separation method, the so-called generalized needlet internal linear combination (GNILC) method, which uses spatial information (the angular power spectra) to disentangle the Galactic dust emission and CIB anisotropies. We produce significantly improved all-sky maps of *Planck* thermal dust emission, with reduced CIB contamination, at 353, 545, and 857 GHz. By reducing the CIB contamination of the thermal dust maps, we provide more accurate estimates of the local dust temperature and dust spectral index over the sky with reduced dispersion, especially at high Galactic latitudes above $b = \pm 20°$. We find that the dust temperature is $T = (19.4 \pm 1.3)$ K and the dust spectral index is $\beta = 1.6 \pm 0.1$ averaged over the whole sky, while $T = (19.4 \pm 1.5)$ K and $\beta = 1.6 \pm 0.2$ on 21% of the sky at high latitudes. Moreover, subtracting the new CIB-removed thermal dust maps from the CMB-removed *Planck* maps gives access to the CIB anisotropies over 60% of the sky at Galactic latitudes $|b| > 20°$. Because they are a significant improvement over previous *Planck* products, the GNILC maps are recommended for thermal dust science. The new CIB maps can be regarded as indirect tracers of the dark matter and they are recommended for exploring cross-correlations with lensing and large-scale structure optical surveys. The reconstructed GNILC thermal dust and CIB maps are delivered as *Planck* products.

Key words. cosmology: observations – methods: data analysis – ISM: general – dust, extinction – infrared: diffuse background – large-scale structure of Universe

1. Introduction

The various populations of dust grains in the Galaxy are heated by absorbing the ultraviolet emission from stars. By re-emitting the light at infrared frequencies, the heated dust grains are responsible for the thermal dust radiation of the Galaxy. For this reason, the dust emission is a tracer of the gas and particle density in the interstellar medium (Planck Collaboration XIX 2011; Planck Collaboration XI 2014; Planck Collaboration Int. XVII 2014; Planck Collaboration Int. XXVIII 2015; Planck Collaboration Int. XXXI 2016) and of the star formation activity in the Galaxy (Draine & Li 2007). The Galactic thermal dust emission is also one of the major astrophysical foregrounds for observations of the cosmic microwave background (CMB) (Planck Collaboration Int. XXX 2016; BICEP2/Keck Array and Planck Collaborations 2015). Incorrect modelling of thermal dust might be responsible for a significant bias on the cosmological parameters (e.g., Remazeilles et al. 2016). The characterization of Galactic thermal dust emission over the whole sky is therefore essential for the accurate subtraction of this foreground from the CMB observations. Accurate characterization of the Galactic dust is also useful for the analysis of supernovae observations, where the Galactic dust causes extinction (Riess et al. 1996).

* Corresponding author: M. Remazeilles,
e-mail: mathieu.remazeilles@manchester.ac.uk

An unresolved background of dusty star-forming early galaxies also generates diffuse emission, known as the cosmic infrared background radiation (Puget et al. 1996; Gispert et al. 2000; Lagache et al. 2005). The cosmic infrared background (CIB) anisotropies are a probe of star formation history in the Universe and also an indirect tracer of the dark matter (Planck Collaboration XVIII 2011; Planck Collaboration XXX 2014). At high frequencies ($\gtrsim$300 GHz), the Galactic thermal dust emission and the CIB radiation both scale approximately as modified blackbodies. This makes it challenging to separate the dust and CIB components solely on the basis of their spectral properties (Planck Collaboration XI 2014; Planck Collaboration X 2016)

The previously released *Planck*[1] dust maps – the *Planck* 2013 (P13) dust model (Planck Collaboration XI 2014) and the *Planck* 2015 (P15) dust model (Planck Collaboration X 2016) – have been produced by fitting a modified blackbody (MBB) spectrum to the *Planck* data. For the P13 dust map, a standard χ^2 fitting of the MBB spectrum was applied pixel by pixel to four maps, namely the CMB-removed *Planck* temperature maps at 353, 545, and 857 GHz from the *Planck* 2013 data release (hereafter PR1), and a 100 μm map obtained from a combination of the IRIS map from Miville-Deschênes & Lagache (2005) and the map from Schlegel et al. (1998). The CMB removal in the *Planck* frequency channels was performed by subtracting the *Planck* SMICA CMB map (Planck Collaboration XII 2014) from the *Planck* frequency maps. For the P15 dust map, a Bayesian fitting of the MBB spectrum was implemented on the *Planck* 2015 data release (hereafter PR2) temperature maps by using the full set of *Planck* frequency channels.

However, the *Planck* dust models P13 and P15 still suffer from contamination by the CIB anisotropies. In particular, at high Galactic latitudes the contamination by CIB anisotropies adds significant uncertainty to the measured dust spectral index and dust temperature (Planck Collaboration XI 2014).

By definition, the spectral fitting employed in Planck Collaboration XI (2014) and Planck Collaboration X (2016) relied solely on the frequency information to reconstruct the Galactic thermal dust model from observations of the sky emission. Because the Galactic dust emission and the extragalactic CIB emission have such similar spectral indices in the *Planck* bands, the result of these frequency-based fits is that the CIB anisotropies inevitably leak into the *Planck* dust model maps. In order to disentangle the Galactic thermal dust emission and the extragalactic CIB emission, additional discriminating statistical information is required.

The CIB temperature fluctuations have been successfully measured by *Planck* in relatively small regions of the sky, where the Galactic dust contamination is low (Planck Collaboration XXX 2014), and the angular power spectra of the CIB anisotropies have been computed at frequencies from 143 GHz to 3000 GHz.

In this work we perform the separation of the Galactic thermal dust and CIB components over a large area of the sky by exploiting not only the frequency spectral information, but also the spatial information through the use of the *Planck* CIB best-fit angular power spectra computed in Planck Collaboration XXX (2014, hereafter CIB 2013). The CIB power spectrum scales approximately as ℓ^{-1} (Planck Collaboration XVIII 2011), while the dust power spectrum scales approximately as $\ell^{-2.7}$ (Planck Collaboration XXX 2014). This distinct spatial behaviour provides the necessary extra statistical information that enables robust separation of thermal dust emission and CIB radiation. Although the CIB 2013 angular power spectra have only been estimated in small areas of the sky, we assume that the statistics of the CIB anisotropies are the same in a larger area of the sky, because of the homogeneity and isotropy of the CIB emission.

The component-separation method employed in this work is the generalized needlet internal linear combination (GNILC) method, first developed in Remazeilles et al. (2011b). It is worth noting that the GNILC method has also been applied in a different context to simulations of a radio intensity mapping experiment for separating the cosmological H I 21-cm temperature fluctuations and the Galactic synchrotron radiation in Olivari et al. (2016), where the component-separation problem was similar.

This paper is organized as follows. In Sect. 2 we present the data used in the analysis. In Sect. 3 we give a summary of the component-separation method that we implement on the data to disentangle the Galactic dust emission and the CIB anisotropies; the full description of the method and validation on simulations are presented in Appendix A. In Sect. 4 we discuss the results for the Galactic thermal dust emission and the estimated spectral parameters. In Sect. 5 we discuss the results for the CIB emission. In Sect. 6 we explore the correlations of the new dust and CIB maps with the H I gas tracer. We conclude in Sect. 7.

2. Data and preprocessing

2.1. Planck data

The data used in this paper are the temperature full-mission sky maps (Planck Collaboration VI 2016; Planck Collaboration VIII 2016) of the *Planck* 2015 data release (PR2) that have been made publicly available on the *Planck* Legacy Archive. We make use of the nine single-frequency maps from 30 to 857 GHz from both LFI and HFI instruments. As discussed in Planck Collaboration XIV (2014), the zodiacal light emission is removed from the *Planck* HFI temperature maps (100 to 857 GHz) by fitting different *Planck* surveys of the sky with the COBE/DIRBE[2] zodiacal model (Kelsall et al. 1998). Because different *Planck* surveys are taken at different times, the sky is observed through different column depths of interplanetary dust. Differencing two surveys removes all distant structure in the maps, such as Galactic and extra-galactic emission, but leaves a detectable Zodiacal signal. This difference signal is fit to extend the COBE zodiacal model to *Planck* frequencies. The entire, un-differenced signal is then reconstructed from the model and removed from the data of each *Planck* HFI bolometer prior to mapmaking (Planck Collaboration VIII 2016).

We also make use of the *Planck* temperature half-mission sky maps (hereafter HM1 and HM2, as defined in Planck Collaboration VIII 2016) in the nine frequency channels, in order to estimate by their half-difference (see Eq. (A.14)) the local rms of the instrumental noise in the *Planck* full-mission maps.

[1] *Planck* (http://www.esa.int/Planck) is a project of the European Space Agency (ESA) with instruments provided by two scientific consortia funded by ESA member states and led by Principal Investigators from France and Italy, telescope reflectors provided through a collaboration between ESA and a scientific consortium led and funded by Denmark, and additional contributions from NASA (USA).

[2] Cosmic Background Explorer Diffuse Infrared Brightness Experiment.

2.2. The IRAS 100 μm map

Following Planck Collaboration XI (2014), in addition to the *Planck* PR2 data we also use in this work the full-sky temperature map at 100 μm based on the combination of the IRIS map (Miville-Deschênes & Lagache 2005) and the map of Schlegel et al. (1998, hereafter SFD map) both projected on the `HEALPix` grid (Górski et al. 2005) at $N_{\rm side} = 2048$. The combined 100 μm map is compatible with the SFD map at angular scales larger than 30′ and compatible with the IRIS map at smaller angular scales. The effective beam resolution of the combined 100 μm map is 4.3′ and the noise rms level is 0.06 MJy sr^{-1}.

It should be noted that residual low-level zodiacal light emission is present in the combined 100 μm map because the zodiacal emission has not been corrected in the same way in the SFD map and in the IRIS map. We refer to the appendix of Planck Collaboration XI (2014) for further discussion of this point.

2.3. Preprocessing of the point sources

We make use of nine point source masks, one for each *Planck* frequency channel, in order to remove the point sources detected in each frequency at a signal-to-noise ratio $S/N > 5$ in the second *Planck* Catalogue of Compact Sources, PCCS2 (Planck Collaboration XXVI 2016).

The masked pixels in each *Planck* frequency map are filled in through a minimum curvature spline surface inpainting technique, implemented in the *Planck* Sky Model (`PSM`) software package (Delabrouille et al. 2013) and described in Remazeilles et al. (2015) and Planck Collaboration XII (2016). For consistency, we also consider the source-subtracted version of the combined 100 μm map that is described in the appendix of Planck Collaboration XI (2014). The inpainted *Planck* 2015 maps and the inpainted combined 100 μm map are the inputs to the component-separation algorithm described in the next section.

3. Summary of the component-separation method

The component-separation technique that we follow in this work is based on Remazeilles et al. (2011b) and called `GNILC`.

In order to simplify the reading of the paper, we give a brief summary of the method employed in this work to separate the thermal dust and CIB anisotropies. A complete description of the formalism and technical details of `GNILC` are presented in Appendix A.

Each frequency map is first decomposed on a needlet (spherical wavelet) frame (Narcowich et al. 2006; Guilloux et al. 2009). The localization properties of the needlets allow us to adapt the component separation to the local conditions of contamination in both harmonic space and real space (Delabrouille et al. 2009; Remazeilles et al. 2011b; Basak & Delabrouille 2012; Remazeilles et al. 2013; Basak & Delabrouille 2013). We define ten needlet windows, $\{h^{(j)}(\ell)\}_{1\leq j\leq 10}$, having a Gaussian shape and acting as bandpass filters in harmonic space, each of them selecting a specific subrange of angular scales (see Fig. A.2). The spherical harmonic transform, $a_{\ell m}$, of each frequency map is bandpass filtered in harmonic space by the ten needlet windows. The inverse transform of the bandpass-filtered coefficient, $h^{(j)}(\ell)a_{\ell m}$, provides a needlet map at scale j, conserving only statistical information from the range of ℓ considered. Therefore, we have 100 input maps (10 frequencies times 10 needlet scales). The component separation is performed on each needlet scale independently. The main steps of the `GNILC` algorithm are the following. For each needlet scale, j, considered we perform seven steps:

1. We compute the frequency-frequency data covariance matrix, at pixel p, and scale j,
$$\widehat{\mathsf{R}}^{j}_{ab}(p) = \sum_{p'\in\mathcal{D}(p)} \boldsymbol{x}^{j}_{a}(p)(\boldsymbol{x}^{j}_{b}(p))^{\mathsf{T}}, \tag{1}$$
where $\mathcal{D}(p)$ is a domain of pixels centred at pixel p and $\boldsymbol{x}^{j}_{a}(p)$ and $\boldsymbol{x}^{j}_{b}(p)$ are the needlet maps at scale j of the observations for the pair of frequencies a, b. In practice, the domain of pixels, $\mathcal{D}(p)$, is defined by the convolution in real space of the product of the needlet maps with a Gaussian kernel. The width of the Gaussian kernel is a function of the needlet scale considered.
2. Similarly, we compute the frequency-frequency covariance matrix of the instrumental noise, at pixel p, and scale j,
$$\widehat{\mathsf{R}}^{j}_{\text{noise }ab}(p) = \sum_{p'\in\mathcal{D}(p)} \boldsymbol{n}^{j}_{a}(p)(\boldsymbol{n}^{j}_{b}(p))^{\mathsf{T}}, \tag{2}$$
where the instrumental noise maps, $\boldsymbol{n}(p)$, are estimated from the half-difference of the half-mission HM1 and HM2 *Planck* maps.
3. Similarly, we compute the frequency-frequency covariance matrix of the CMB, $\widehat{\mathsf{R}}^{j}_{\rm CMB}(p)$, and the frequency-frequency covariance matrix of the CIB, $\widehat{\mathsf{R}}^{j}_{\rm CIB}(p)$, but this time using CMB maps and CIB maps that are simulated from the *Planck* CMB best-fit C_ℓ (Planck Collaboration XV 2014) and the *Planck* CIB best-fit $C_\ell^{a\times b}$ (Planck Collaboration XXX 2014) respectively. The simulated maps were analyzed with the same needlet decomposition as was applied to the real data before computing the CMB and CIB covariance matrices.
4. We compute the "nuisance" covariance matrix, $\widehat{\mathsf{R}}_{\rm N}$, by co-adding the noise covariance matrix, the CMB covariance matrix, and the CIB covariance matrix:
$$\widehat{\mathsf{R}}_{\rm N} = \widehat{\mathsf{R}}_{\rm CIB} + \widehat{\mathsf{R}}_{\rm CMB} + \widehat{\mathsf{R}}_{\rm noise}. \tag{3}$$
5. We diagonalize the transformed data covariance matrix
$$\widehat{\mathsf{R}}_{\rm N}^{-1/2}\widehat{\mathsf{R}}\,\widehat{\mathsf{R}}_{\rm N}^{-1/2} = \widehat{\mathsf{U}}\begin{bmatrix} \mu_1 & & \\ & \dots & \\ & & \mu_{N_{\rm ch}} \end{bmatrix}\widehat{\mathsf{U}}^{\mathsf{T}} \approx \widehat{\mathsf{U}}_{\rm S}\widehat{\mathsf{D}}_{\rm S}\widehat{\mathsf{U}}_{\rm S}^{\mathsf{T}} + \widehat{\mathsf{U}}_{\rm N}\widehat{\mathsf{U}}_{\rm N}^{\mathsf{T}}, \tag{4}$$
where $N_{\rm ch}$ is the number of frequency channels. In this representation, the eigenvalues that are close to unity correspond to the nuisance power (CIB plus CMB plus noise), while the m eigenvalues larger than unity that are collected in the diagonal matrix $\widehat{\mathsf{D}}_{\rm S}$ correspond to the power of the Galactic signal. The matrix $\widehat{\mathsf{U}}_{\rm S}$ collects the m eigenvectors spanning the Galactic signal subspace.
6. We compute the effective dimension, m, of the foreground signal subspace (number of Galactic degrees of freedom, or principal components) by minimizing the Akaike Information Criterion (AIC, Akaike 1974):
$$\min_{m\in[1,N_{\rm ch}]}\left(2\,m + \sum_{i=m+1}^{N_{\rm ch}}(\mu_i - \log\mu_i - 1)\right), \tag{5}$$
where μ_i are the eigenvalues of $\widehat{\mathsf{R}}_{\rm N}^{-1/2}\widehat{\mathsf{R}}\,\widehat{\mathsf{R}}_{\rm N}^{-1/2}$.

7. We apply the m–dimensional ILC filter (Remazeilles et al. 2011b) to the data in order to reconstruct the total Galactic signal at scale j:

$$\widehat{\boldsymbol{f}}^{j} = \widehat{\mathsf{F}}\left(\widehat{\mathsf{F}}^{\mathsf{T}}\widehat{\mathsf{R}}^{-1}\widehat{\mathsf{F}}\right)^{-1}\widehat{\mathsf{F}}^{\mathsf{T}}\widehat{\mathsf{R}}^{-1}\boldsymbol{x}^{j}, \quad (6)$$

where the estimated mixing matrix is given by

$$\widehat{\mathsf{F}} = \widehat{\mathsf{R}}_{\mathrm{N}}^{1/2}\widehat{\mathsf{U}}_{\mathrm{S}} \quad (7)$$

with $\widehat{\mathsf{U}}_{\mathrm{S}}$ collecting the m eigenvectors selected by the AIC criterion at scale j.

The reconstructed Galactic signal maps are finally synthesized as follows. We transform the estimated maps, $\widehat{\boldsymbol{f}}^{j}$, to spherical harmonic coefficients, then bandpass filter the harmonic coefficients by the respective needlet window, h_{ℓ}^{j}, and transform back to maps in real space. This operation provides one reconstructed Galactic signal map per needlet scale. We co-add these maps to obtain, for each frequency channel, the complete reconstructed Galactic signal map on the whole range of angular scales. The needlet windows are chosen so that $\sum_{j=1}^{10}\left(h_{\ell}^{j}\right)^{2} = 1$, therefore conserving the total power in the synthesis.

The reconstruction of the CIB maps is performed as follows. In step 4, we replace Eq. (3) by $\widehat{\mathsf{R}}_{\mathrm{N}} = \widehat{\mathsf{R}}_{\mathrm{CMB}} + \widehat{\mathsf{R}}_{\mathrm{noise}}$ so that the reconstructed signal is the sum of the Galactic dust plus the CIB. We then subtract the reconstructed Galactic dust (only), $\widehat{\boldsymbol{f}}$, from the Galactic dust plus CIB reconstruction.

It should be noted that the priors on the CMB and CIB angular power spectra are only used for estimating the dimension, m, of the Galactic signal subspace (step 5), not for the ILC filtering (step 7) in the reconstruction of the components of the emission.

We have validated the GNILC method on the *Planck* full focal plane simulations (Planck Collaboration XII 2016) before applying it to the *Planck* data. The results on simulations are presented in Sect. A.6 of Appendix A.

4. GNILC results on the thermal dust

4.1. Dust maps and power spectra

In Fig. 1 we compare various maps projected onto a high Galactic latitude 12.°5 × 12.°5 area centred at $(l, b) = (90°, -80°)$. In the top left panel of Fig. 1, the *Planck* 353-GHz channel map is shown. At 353 GHz the CMB radiation is clearly visible in the *Planck* observation map at high Galactic latitude, through degree-scale temperature fluctuations which are typical in size of the CMB anisotropies. In the top right panel of Fig. 1, the *Planck* 353-GHz map is shown after subtraction of the *Planck* CMB map (i.e. the SMICA map from Planck Collaboration XII 2014). The CMB-removed *Planck* 353-GHz map reveals the thermal dust emission, but is still quite noisy and contaminated by the CIB temperature anisotropies. The dust model P13 at 353 GHz, which has been computed by fitting an MBB spectrum to the CMB-removed *Planck* maps (Planck Collaboration XI 2014), is plotted in the middle left panel of Fig. 1. Because of the similar spectral signatures of the thermal dust and the CIB, the dust model P13 resulting from the spectral fitting can not avoid the leakage of the CIB fluctuations into the dust map. Conversely, in the GNILC dust map at 353 GHz produced in this work, the CIB anisotropies have been successfully filtered out, while the 5′-scale dust emission has been conserved in the map. All the maps are shown at 5′ resolution, but the GNILC dust map has a local effective beam resolution that is shown in Fig. 2. The local beam resolution of the GNILC dust maps is not the result of a local smoothing of the maps, but the result of the thresholding of the needlet coefficients that depends on local signal-to-noise ratio. In some high-latitude regions of the sky, beyond a certain angular scale, the power of the dust is found to be consistent with zero, i.e. the dimension of the Galactic signal subspace selected by the AIC criterion is $m = 0$ (see Fig. A.1) because the sky observations in this needlet domain become compatible with the CIB-plus-CMB-plus-noise model.

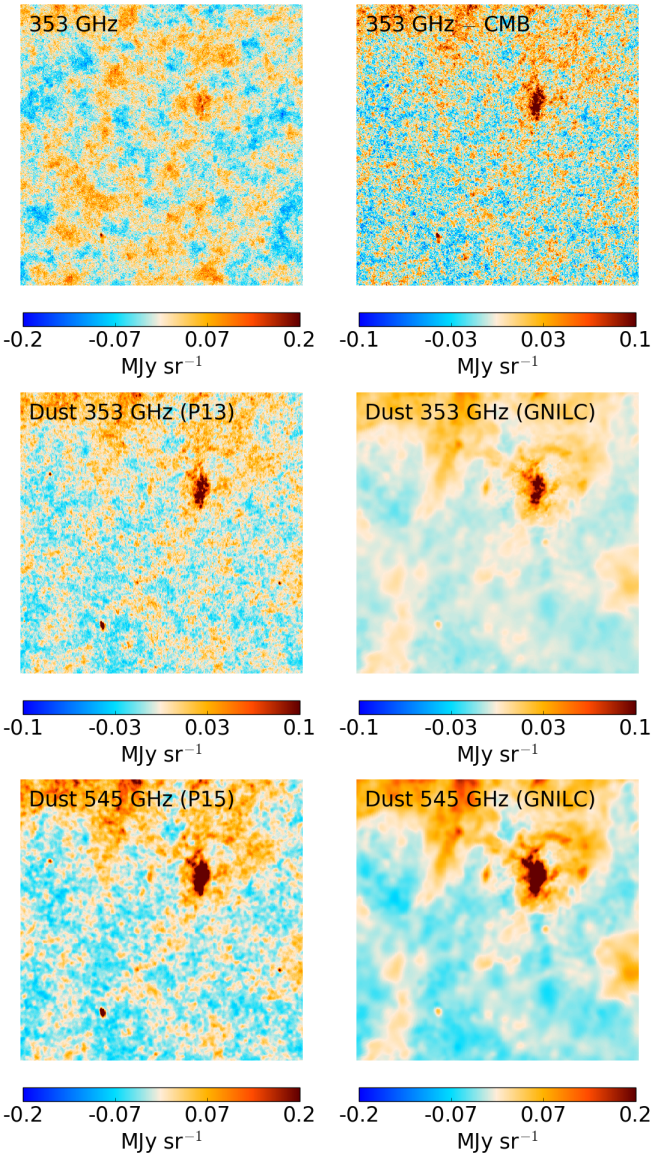

Fig. 1. 12.°5 × 12.°5 gnomonic projection of the sky centred at high latitude $(l, b) = (90°, -80°)$. *Top left*: *Planck* 353-GHz map. *Top right*: CMB-removed *Planck* 353-GHz map. *Middle left*: dust model P13 at 353 GHz (MBB fit on CMB-removed *Planck* maps). *Middle right*: GNILC dust map at 353 GHz. *Bottom left*: dust model P15 at 545 GHz (Commander Bayesian fitting). *Bottom right*: GNILC dust map at 545 GHz. Maps at 353 GHz are shown at 5′ resolution, while maps at 545 GHz are smoothed to 7.5′ resolution. The GNILC dust maps have a non-uniform resolution (see Fig. 2) with 5′ resolution kept in regions of bright dust emission. In each image the local mean intensity has been subtracted for this comparison.

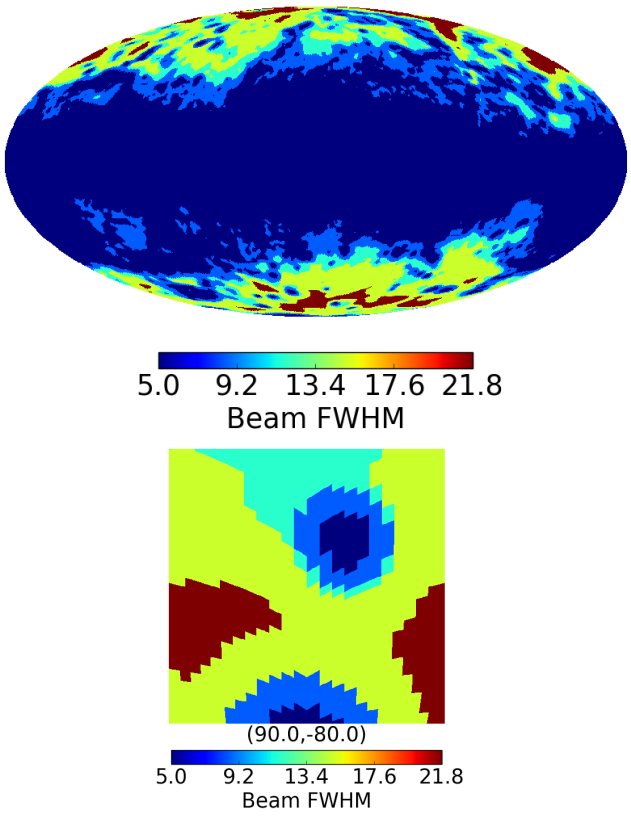

Fig. 2. Effective beam FWHM of the GNILC dust maps on the whole sky (*top panel*) and on a 12.°5 × 12.°5 area of the sky centred at high latitude $(l, b) = (90°, -80°)$ (*bottom panel*). The spatially varying beam FWHM is the same for all frequencies. GNILC preserves the 5′-scale power of the thermal dust in the high signal-to-noise regions of the sky.

In the bottom panels of Fig. 1, we compare the dust model P15 at 545 GHz from Planck Collaboration X (2016) and the GNILC dust map at 545 GHz produced in this work. The dust model P15 has been obtained by using a Bayesian fitting method, Commander (Eriksen et al. 2008), instead of the χ^2 fitting method used for the dust model P13 in Planck Collaboration XI (2014). Commander makes an overall fit of many foreground parameters, including those of the thermal dust component (intensity, spectral index, and temperature). However, the Commander fitting again does not make any distinction between the CIB and the Galactic thermal dust, both sharing a similar MBB spectrum. In summary, thermal dust and CIB are still fitted as a single component in constructing the dust models P13 and P15. The dust model P15 at 545 GHz still shows CIB anisotropies at high latitude, whereas those CIB anisotropies have been successfully filtered out in the GNILC dust map at 545 GHz (see Fig. 1). Unlike the dust models P13 and P15, the GNILC dust maps are not the result of any fit of a dust model, but the result of a component-separation procedure solely based on prior assumptions on the CIB, CMB, and noise angular power spectra.

Figure 3 shows the GNILC all-sky map of the thermal dust at 353 GHz in the bottom panel. This map can be compared to the dust model P13 at 353 GHz from Planck Collaboration XI (2014), shown in the top panel. While the dust model P13 still shows visible small-scale contamination by CIB anisotropies at high latitude, in the GNILC dust map the CIB fluctuations are clearly filtered out at high latitude. The 12.°5 × 12.°5 gnomonic projections, centred at $(l, b) = (90°, -80°)$, of the various GNILC maps of the dust at 353, 545, and 857 GHz, are shown in Fig. 4.

At high Galactic latitude and small angular scales, the AIC criterion can select a dimension zero for the Galactic signal subspace, considering that in this region the Galactic signal is completely buried under the CIB and noise signals, and therefore the dust is compatible with zero. This aspect of the GNILC filtering is visible in the bottom panel of Fig. A.1, where in the high-latitude region at 5′ scale there are no Galactic degrees of freedom selected by the AIC criterion. Therefore, in practice the GNILC filtering is equivalent to a local smoothing of the sky map, depending on the relative power of the Galactic dust with respect to the local contamination by the CIB, the CMB, and the instrumental noise. The effective local beam FWHM over the sky of the GNILC dust maps is plotted in Fig. 2. Over 65% of the sky, where the dust signal is significant, the 5′ beam resolution is preserved by the GNILC filtering.

It is interesting to look at the residual map given by the difference between the CMB-removed *Planck* map and the dust map, i.e. the difference map (*Planck* map − *Planck* CMB map − dust map). In the case where the GNILC dust map is used in the subtraction, the residual map clearly shows the CIB anisotropies plus the instrumental noise (left panel of Fig. 5), as expected. Conversely, if the *Planck* 2103 dust model is used for the subtraction in place of the GNILC dust map then the residual map shows the instrumental noise only (middle panel of Fig. 5). This, again, indicates that the CIB anisotropies have leaked into the dust model P13, and therefore that the CIB anisotropies can not be recovered in the residual map. In the right panel of Fig. 5, we plot the difference between the *Planck* 2103 dust model and the GNILC dust map at 353 GHz, highlighting the amount of CIB leaking into the dust model P13.

The resulting angular power spectrum of the various dust maps and the residual maps at 353, 545, and 857 GHz are plotted in Fig. 6. We have used the HEALPix routine anafast (Górski et al. 2005) for computing the angular power spectrum of the maps. The amplitude of the power spectrum of the GNILC dust map at 353 GHz (long dashed red line) is reduced by a factor of 2 at $\ell \approx 1000$ with respect to the dust model P13 (dotted blue line) because of the removal of the CIB contamination. The power spectrum of the GNILC dust map is steeper than the power spectrum of the dust model P13. The GNILC dust power spectrum scales as a power-law $C_\ell \approx \ell^{-2.7}$. For completeness, the GNILC dust power spectrum corrected for residual noise is overplotted as a solid green line.

The angular power spectrum of the GNILC residual map, i.e. of the difference map (*Planck* map − *Planck* CMB − GNILC dust), typically shows the power of the CIB plus noise that has been filtered out in the GNILC dust map (solid yellow line). As illustrated in the top panel of Fig. 6, the angular power spectrum of the GNILC residual map successfully matches the sum of the *Planck* CIB best-fit power spectrum at 353 GHz (dash-dot purple line) and the *Planck* 353-GHz instrument noise power spectrum (dashed orange line). At 545 and 857 GHz the angular power spectrum of the GNILC residual map is below the *Planck* CIB best-fit power spectrum, which means that some amount of residual CIB contamination is still left in the GNILC dust maps at 545 and 857 GHz.

4.2. Thermal dust temperature and spectral index

Following Planck Collaboration XI (2014), we fit in each pixel a modified blackbody (MBB) spectral model to the GNILC dust maps at 353, 545, 857, and 3000 GHz in order to estimate

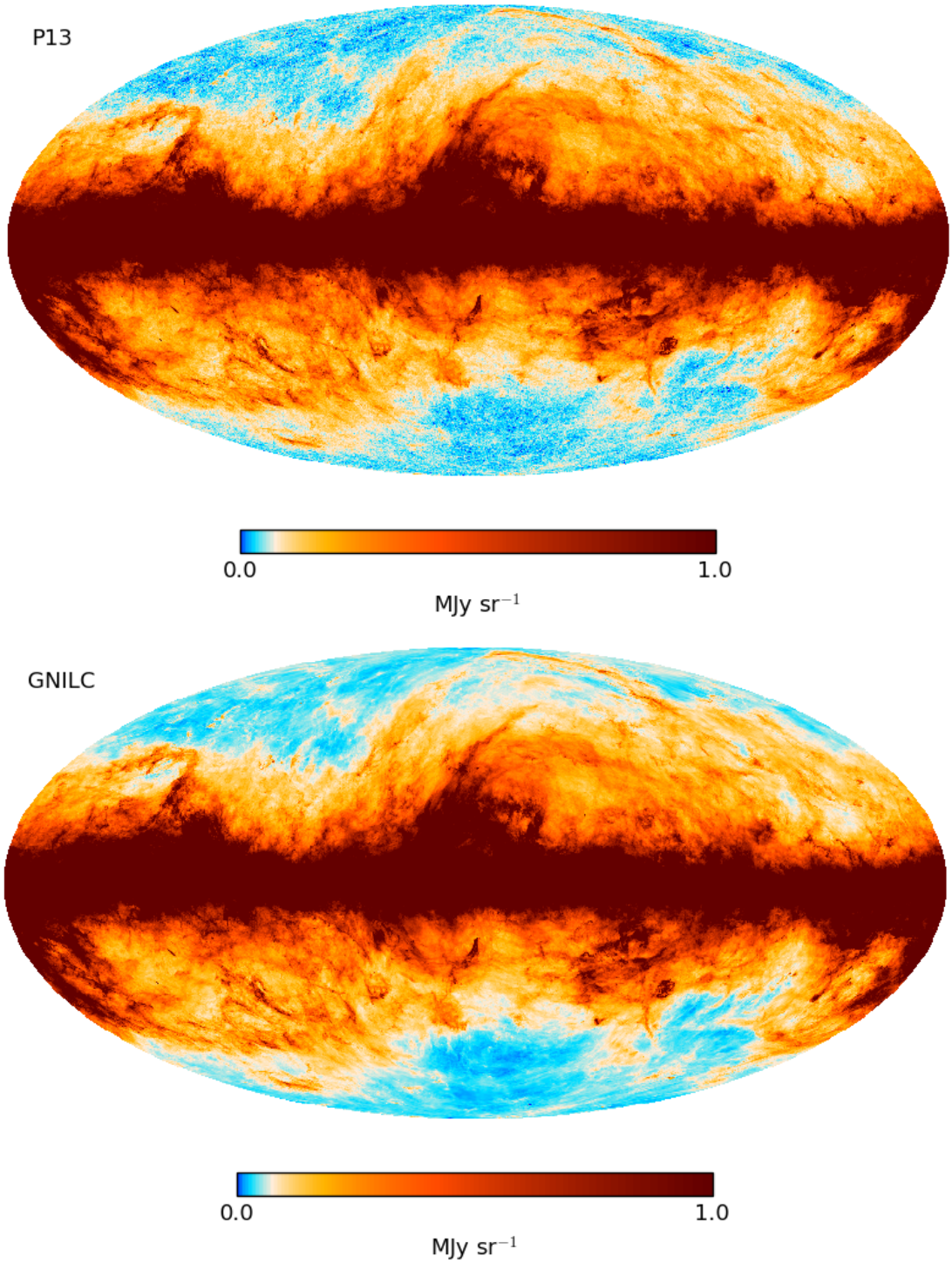

Fig. 3. Full-sky map of the Galactic thermal dust emission: *Planck* 2013 (P13) thermal dust model at 353 GHz and 5′ resolution (*top panel*), suffering from CIB contamination at high latitudes, and the GNILC dust map (this work) at 353 GHz and 5′ resolution (*bottom panel*), for which the CIB is clearly filtered out at high-latitudes. A logarithmic colour scale is used here to highlight the low-intensity emission at high latitudes. The effective local beam of the GNILC dust maps is shown in Fig. 2.

the dust temperature, spectral index, and optical depth over the sky. We also performed an analysis similar to that of Planck Collaboration XI (2014), which used the PR1 data, by fitting the same MBB model to the CMB-removed PR2 maps, in place of the GNILC dust maps. We refer to this as the PR2 MBB fit. This allows us to highlight the improvement in estimating the dust temperature and spectral index after filtering out the CIB anisotropies with GNILC.

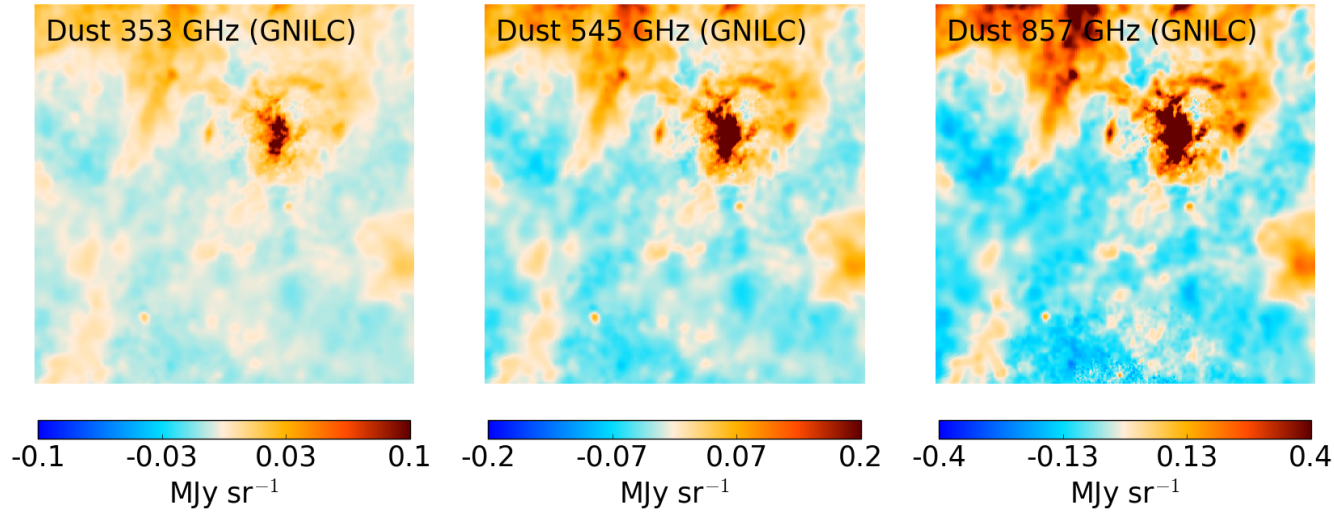

Fig. 4. GNILC dust maps at 353 GHz (*left panel*), 545 GHz (*middle panel*), and 857 GHz (*right panel*) on a 12.°5 × 12.°5 gnomonic projection of the sky centred at high latitude, $(l, b) = (90°, -80°)$. GNILC filters out the CIB anisotropies while preserving the small-scale dust signal (see bottom panel of Fig. 2). In these images, the local mean intensity of each map has been subtracted.

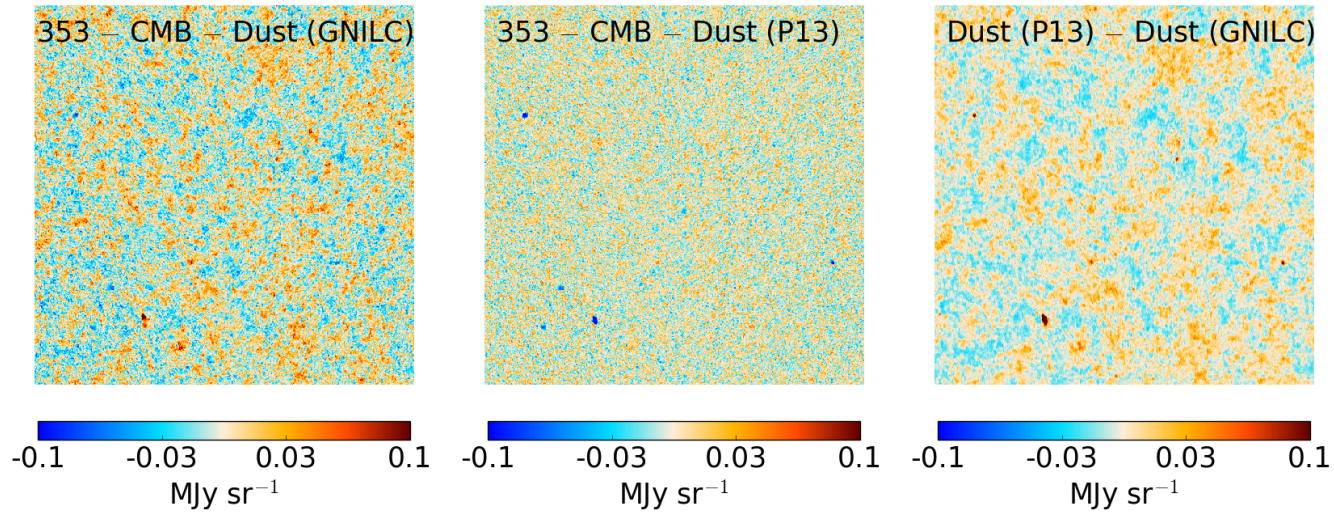

Fig. 5. 12.°5 × 12.°5 gnomonic projection of the sky centred at high latitude, $(l, b) = (90°, -80°)$. *Left*: difference map (*Planck* 353 GHz − *Planck* CMB − GNILC dust) reveals the CIB anisotropies at 353 GHz. *Middle*: difference map (*Planck* 353 GHz − *Planck* CMB − dust model P13) revealing only the instrumental noise because the dust model P13, like the *Planck* observations at 353 GHz, still contains the CIB signal. *Right*: difference (dust model P13 − GNILC dust) revealing the amount of CIB contamination in the dust model P13 with respect to the GNILC dust map. In these images, the local mean intensity of each map has been subtracted.

4.2.1. χ^2 fitting

The model of dust emission that we fit to the data is a modified blackbody (MBB) spectrum with three parameters:

$$I_\nu(p) = \tau_0(p)\,(\nu/\nu_0)^{\beta(p)}\,B_\nu\,(T(p))\,, \tag{8}$$

where $\nu_0 = 353$ GHz is the reference frequency, $\tau_0(p)$ the dust optical depth at 353 GHz in pixel p, $T(p)$ the dust temperature in pixel p, and $\beta(p)$ the dust spectral index in pixel p. The function $B_\nu\,(T)$ is the Planck law for blackbody radiation.

We use a standard χ^2 fitting method as in Planck Collaboration XI (2014). However, there a two-step approach was adopted for the fit; in order to limit the fluctuations in the estimated parameters induced by the noise and the CIB contamination, the spectral index parameter was estimated at 30′ resolution in a first step, then the temperature and the optical depth were fit at 5′ resolution. Given that we already have cleaned the thermal dust from CIB contamination at 353, 545, 857, and 3000 GHz by using the GNILC component-separation method, there is no reason to perform a low-resolution MBB fit on the cleaned GNILC maps. Therefore, we will fit the three parameters τ_0, β, and T simultaneously at full resolution (5′), instead of following the two-step approach adopted in Planck Collaboration XI (2014). For the fit, we use the frequency data at 353, 545, 857, and 3000 GHz, either from the unfiltered PR2 data (i.e. inputs similar to those used to produce the dust model P13) or from the CIB-removed GNILC dust maps. In this way, we will highlight the improvement in the estimated dust parameters resulting from the removal of the CIB fluctuations with GNILC.

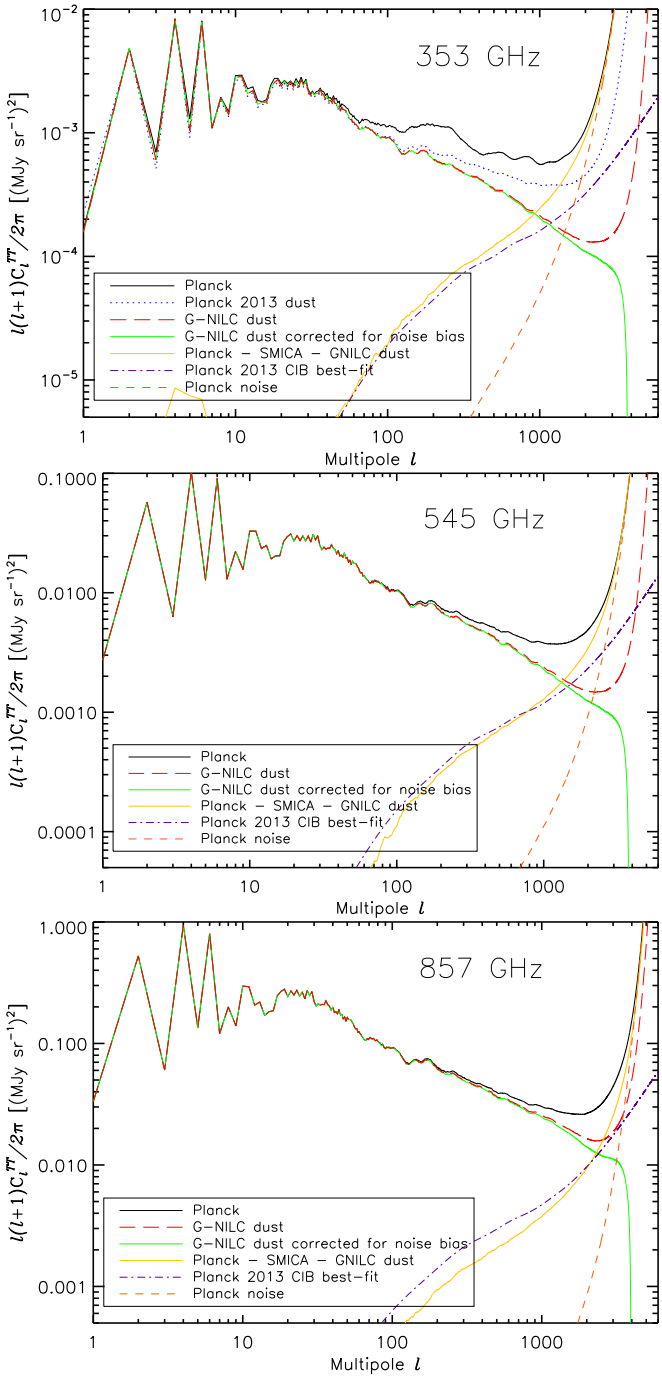

Fig. 6. Angular power spectra of the various maps at 353 GHz (*top panel*), 545 GHz (*middle panel*), and 857 GHz (*bottom panel*), on a fraction of the sky, $f_{\rm sky}$ = 57%: *Planck* map (solid black line), dust model P13 (dotted blue line, Planck Collaboration XI 2014), GNILC dust map (long dashed red line), GNILC dust map corrected for the residual noise (solid green line), and GNILC residual map (*Planck* map − *Planck* CMB − GNILC dust, solid yellow line), which is compared to the *Planck* CIB best-fit power spectrum (dash-dot purple line, Planck Collaboration XXX 2014) and the *Planck* noise power spectrum (dashed orange line).

In most of the images presented in this paper the local average of the dust maps has been subtracted to facilitate side-by-side comparisons of the different versions of the *Planck* dust map in terms of contamination by CIB fluctuations. There is no subtraction of any offset in the released GNILC products themselves. In order to fit for the dust spectral parameters, τ_0, T, and β, the offsets of the GNILC dust maps have been estimated by correlation with the H I map at high latitude in the exact same way as described in Planck Collaboration XI (2014). The offsets of the GNILC dust maps are found to be 0.1248, 0.3356, 0.5561, and 0.1128 MJy sr^{-1} at 353, 545, 857, and 3000 GHz respectively. The uncertainties on the absolute calibration of the *Planck* channels have been estimated from the observation of planets (Planck Collaboration VIII 2016); they are 1.2% at 353 GHz, 6.3% at 545 GHz, and 6.1% at 857 GHz. The calibration incertainty at 3000 GHz is 13.5% (Miville-Deschênes & Lagache 2005). Calibration uncertainties and offset uncertainties have been taken into account in the χ^2 fitting, following the procedure detailed in the appendix of Planck Collaboration XI (2014).

4.2.2. Parameter maps

The results of the MBB fit to the GNILC dust maps are shown on the left panels of Fig. 7. The estimated GNILC temperature map and GNILC spectral index map are compared to the PR2 MBB fit temperature map and the PR2 MBB fit spectral index map at 5′ resolution. The PR2 MBB fit is similar to the dust model P13 of Planck Collaboration XI (2014), i.e. the CIB anisotropies have not been filtered out, except that the model fitting is applied to the PR2 data instead of the PR1 data and not performed in two steps, but carried out simultaneously for the three dust parameters at 5′ resolution. The impact of the CIB contamination on the measurement of the dust temperature and dust spectral index is particularly significant at high latitude in the PR2 MBB fit.

In the bottom panels of Fig. 7, we plot the resulting χ^2 map of both the GNILC MBB fit and the PR2 MBB fit. This provides a direct measurement of the goodness-of-fit. The reason for some reduced χ^2 values being smaller than unity is mostly that calibration uncertainties are included per pixel in the fit, to give less weight to data points with larger uncertainty (Planck Collaboration XI 2014). However, the exact scale of χ^2 is not relevant here, what is important is that the pixel-to-pixel differences in the goodness-of-fit are strongly reduced for the GNILC MBB fit because of the removal of the CIB contamination in the GNILC dust maps. Clearly, the CIB-filtered GNILC maps lead to a better fitting of the MBB model over the sky than the unfiltered PR2 maps. Near the Galactic plane, the χ^2 values between the GNILC MBB fit and the unfiltered PR2 MBB fit are consistent because the CIB contamination plays a negligible role where the dust emission is bright. For a given spectral model of thermal dust, here a single MBB model, the GNILC maps provide higher precision than the unfiltered PR2 maps because of the removal of CIB fluctuations prior to fitting. However, the MBB model might not be the best parametrization of the thermal dust emission in the inner Galactic plane region, which shows high values of the χ^2 statistic for both PR2 and GNILC fits. It is likely that multiple MBB components of dust might contribute to the emission along the line of sight, in which case the exact parametrization of the thermal dust spectral energy distribution in the inner Galactic plane region is not trivial and might need more than three effective parameters.

In Figs. 8 and 9 we compare the GNILC and PR2 MBB fit for temperature and spectral index respectively, at low and high latitudes in the sky. The improvement from GNILC in terms of the reduction of the CIB contamination is particularly visible at high latitude for both temperature and spectral index.

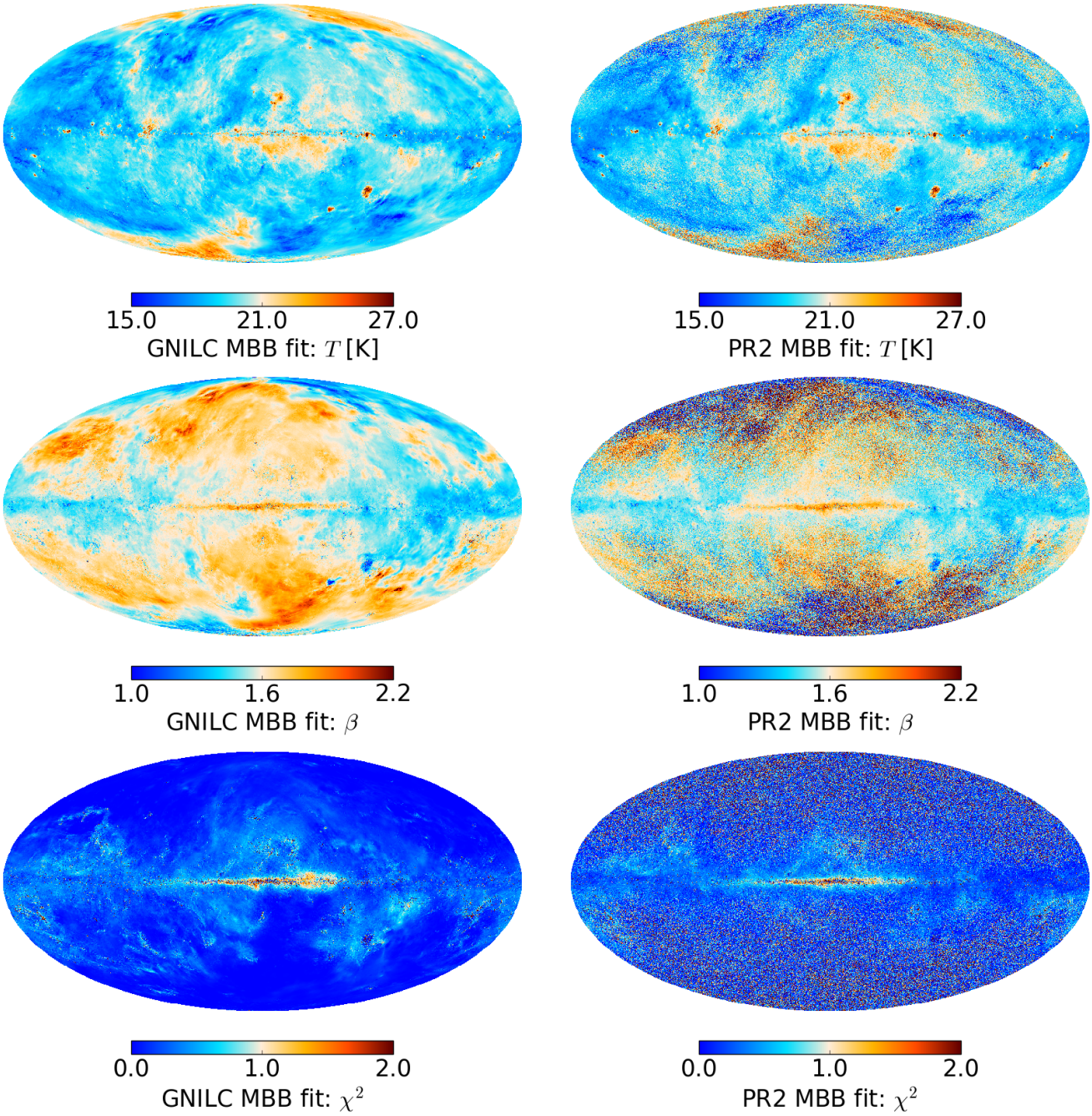

Fig. 7. Full-sky thermal dust parameter maps: temperature (*top row*), spectral index (*middle row*), and map of the χ^2 statistic of the fit (*bottom row*). *Left panels*: GNILC modified blackbody (MBB) fit. *Right panels*: PR2 modified blackbody (MBB) fit a la model P13.

In Fig. 10 we define low- and high-latitude areas of the sky to look at the evolution of the distribution of the dust temperature and spectral index with respect to latitude. Figure 11 shows the normalized histograms of the temperature map, T, and the spectral index map, β, for three different fits: GNILC (red contours); PR2 MBB fit a la model P13 (green contours); and dust model P15 (blue contours). It is important to note that the dust model P15 is a low-resolution Bayesian fit at 60′ resolution with Gaussian priors on T (23 ± 3 K) and β (1.55 ± 0.1). We distinguish three areas in the sky: the high-latitude area defined in Fig. 10, covering 21% of the sky (top panels); the low-latitude area defined in Fig. 10, covering 20% of the sky (middle panels); and the whole sky (bottom panels). As a complement to Fig. 11, Table 1 summarizes the mean best-fit values of the dust parameters, along with their 1σ errors, for the three different products (GNILC MBB fit, PR2 MBB fit similar to the dust model P13, and dust model P15) in the three different areas of the sky. The histograms in Fig. 11 highlight the impact of the CIB anisotropies on the dust spectral parameters: at high latitude the CIB contamination increases the scatter in the temperature and spectral index distributions. The removal of the CIB anisotropies with GNILC reduces the dispersion in the dust temperature by 40% at high latitude (30% on the whole sky) with respect to the PR2 MBB fit and by 10% with respect to the dust model P15 (Table 1), even

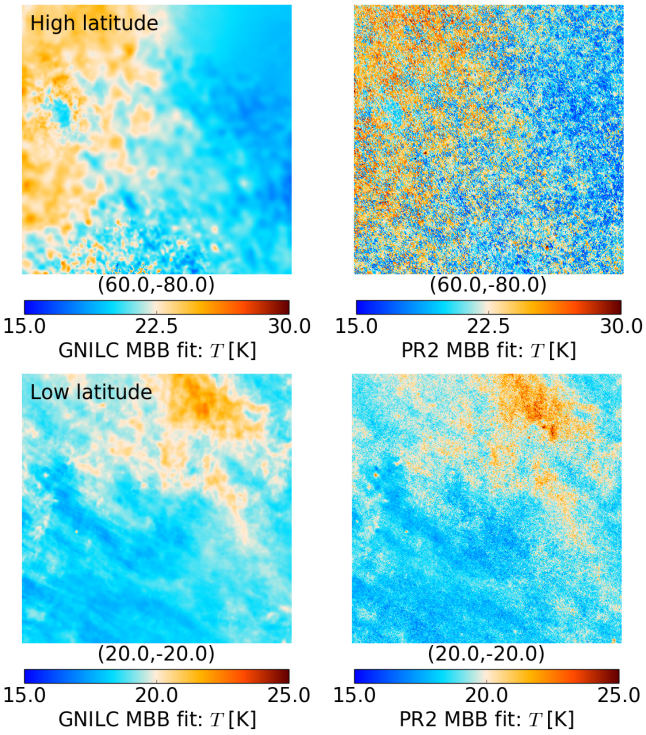

Fig. 8. 12.°5 × 12.°5 gnomonic projections of the dust temperature maps at high latitude, $b = -80°$ (*top panels*) and low latitude, $b = -20°$ (*bottom panels*). *Left*: GNILC MBB fit. *Right*: PR2 MBB fit according to model P13.

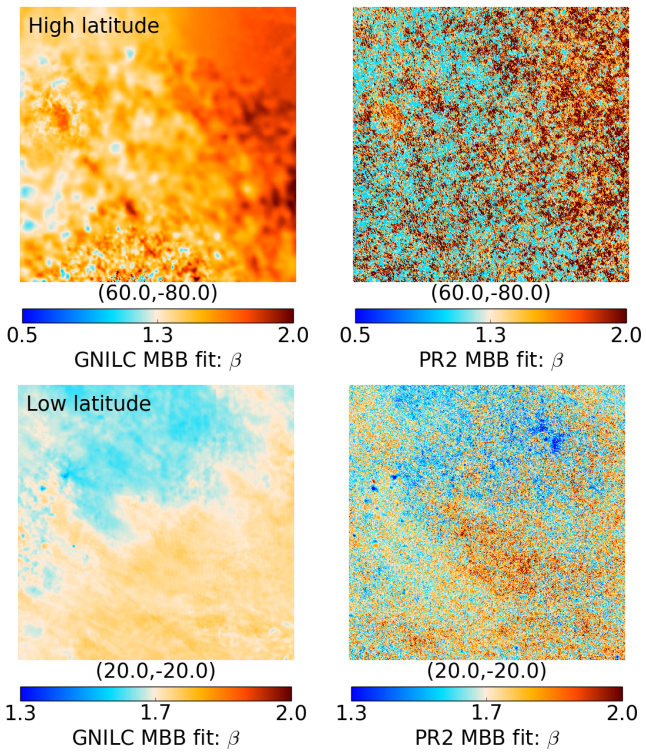

Fig. 9. 12.°5×12.°5 gnomonic projections of the dust spectral index maps at high latitude, $b = -80°$ (*top panels*) and low latitude, $b = -20°$ (*bottom panels*). *Left*: GNILC MBB fit. *Right*: PR2 MBB fit according to model P13.

Fig. 10. High-latitude area of the sky with $f_{\rm sky} = 21\%$ (*top*) and low-latitude area of the sky with $f_{\rm sky} = 20\%$ (*bottom*) that are considered in Fig. 11 and Table 1.

Table 1. Mean and dispersion of the dust temperature and spectral index in different areas of the sky (full sky, high latitude, low latitude). *Top*: GNILC MBB fit. *Middle*: PR2 MBB fit a la dust model P13. *Bottom*: dust model P15 (Commander 60′).

Area	$f_{\rm sky}$ [%]	$\langle T_{\rm GNILC}\rangle$ [K]	$\sigma(T_{\rm GNILC})$ [K]	$\langle\beta_{\rm GNILC}\rangle$	$\sigma(\beta_{\rm GNILC})$
Full sky	100	19.40	1.26	1.60	0.13
High latitude .	21	19.41	1.54	1.63	0.17
Low latitude .	20	19.19	1.49	1.54	0.11
Area	$f_{\rm sky}$ [%]	$\langle T_{\rm PR2}\rangle$ [K]	$\sigma(T_{\rm PR2})$ [K]	$\langle\beta_{\rm PR2}\rangle$	$\sigma(\beta_{\rm PR2})$
Full sky	100	19.50	1.70	1.59	0.27
High latitude .	21	19.56	2.46	1.64	0.45
Low latitude .	20	19.18	1.50	1.55	0.10
Area	$f_{\rm sky}$ [%]	$\langle T_{\rm P15}\rangle$ [K]	$\sigma(T_{\rm P15})$ [K]	$\langle\beta_{\rm P15}\rangle$	$\sigma(\beta_{\rm P15})$
Full sky	100	20.93	2.25	1.54	0.05
High latitude .	21	23.25	1.67	1.55	0.05
Low latitude .	20	18.63	1.96	1.57	0.05

though the P15 temperature fit is smoothed to 60′ resolution. The impact of the CIB removal with GNILC is even more significant for the dust spectral index, with the dispersion reduced by 60% at high latitude (50% on the whole sky) with respect to the PR2 MBB fit. The 1σ error on the P15 spectral index has a lowest value of 0.05 in any area of the sky for two reasons: first, the resolution of the P15 spectral index is much lower (60′); second, a tight prior has been imposed on β in the Commander fit (Planck Collaboration X 2016). With GNILC we find a dust temperature of $T = (19.4 \pm 1.3)$ K and a dust spectral index of $\beta = 1.6 \pm 0.1$ as the best-fit values on the whole sky, where